Convectively Generated Internal Gravity Waves in the Lower Atmosphere of Venus. Part I: No Wind Shear

R. DAVID BAKER* AND GERALD SCHUBERT+

Department of Earth and Space Sciences, University of California, Los Angeles, Los Angeles, California

PHILIP W. JONES

Theoretical Division, Los Alamos National Laboratory, Los Alamos, New Mexico

(Manuscript received 29 July 1998, in final form 10 March 1999)

ABSTRACT

This paper is the first of a two-part study that investigates internal gravity wave generation by convection in the lower atmosphere of Venus. A two-dimensional, nonlinear, fully compressible model of a perfect gas is employed. The calculations consider the lower atmosphere from 12- to 60-km altitude, thereby including two convection regions: the lower atmosphere convection layer from roughly 18- to 30-km altitude and the cloud-level convection layer from roughly 48- to 55-km altitude. The gravity waves of interest are located in the stable layer between these two convection regions. Part I of this study considers gravity wave generation and propagation in the absence of mean wind shear.

In the absence of mean wind shear, internal gravity waves are primarily generated by cloud-level convection. Horizontal wavelengths (~10–15 km) are similar to dominant horizontal scales in the cloud-level penetrative region, and intrinsic horizontal phase speeds are comparable to cloud-level downdraft velocities. Without mean wind shear, there is no effective coupling between the lower atmosphere below 34-km altitude and the overlying stable layer. Simulated wave amplitudes and vertical wavelengths agree well with spacecraft observations, suggesting that gravity waves generated by cloud-level convection through the ''mechanical oscillator'' effect may be responsible for observed variations in the stable layer.

1. Introduction

Internal gravity waves likely occur within the stable layer in Venus's atmosphere from roughly 30- to 48-km altitude. Doppler tracking of the Pioneer Venus North probe reveals oscillations in the stable layer with velocity amplitudes of 2–5 m s^{-1} and a mean vertical wavelength of ~7.5 km (Seiff et al. 1980). Similarly, interferometric radio tracking of Pioneer Venus probes indicates meridional velocity oscillations of ~2 m s^{-1} and vertical wavelengths of ~6–7 km in the stable layer (Counselman et al. 1980; Seiff et al. 1992). Venera 9 and 10 probes also observed velocity oscillations (vertical velocities ~0.3–0.5 m s^{-1}) with slightly larger vertical wavelengths of 10–15 km (Kerzhanovich and Marov 1983). More recently, Magellan radio occultation experiments show temperature oscillations below the cloud-level convection layer (located roughly from 48- to 55-km altitude) with amplitudes of 0.5–1.5 K and vertical wavelengths of about 5–10 km (Jenkins et al. 1994; Hinson and Jenkins 1995). While these oscillations may represent planetary-scale disturbances (Seiff et al. 1992), they may also indicate small-scale internal gravity waves propagating within the stable layer (Seiff et al. 1992; Hinson and Jenkins 1995).

Most theoretical studies of small-scale gravity waves in Venus's atmosphere have focused on vertical wave propagation within and above the clouds (Schubert and Walterscheid 1984; Young et al. 1987, 1994; Leroy 1994; Leroy and Ingersoll 1995, 1996). However, a number of investigations have highlighted the potentially important role of small-scale gravity waves on atmospheric dynamics in the lower atmosphere. Venus's atmosphere exhibits westward zonal winds at all altitudes with a maximum wind speed of 100 m s^{-1} at 65-km altitude. The westward zonal flow is commonly referred to as the Venus atmospheric superrotation (e.g.,

* Current affiliation: NASA Goddard Space Flight Center, Universities Space Research Association, Greenbelt, Maryland.

+ Additional affiliation: Institute of Geophysics and Planetary Physics, University of California, Los Angeles, Los Angeles, California.

Corresponding author address: Dr. R. David Baker, NASA Goddard Space Flight Center, Code 912, Universities Space Research Association, Greenbelt, MD 20771.
E-mail: rbaker@agnes.gsfc.nasa.gov

Schubert 1983; Gierasch et al. 1997). Hou and Farrell (1987) suggested that vertically propagating internal gravity waves forced near the surface, perhaps by boundary layer convection, may help maintain the Venus atmospheric superrotation below 45-km altitude through critical level absorption. In addition, vertically ducted, horizontally propagating gravity waves in the stable layer from 30- to 48-km altitude may transport momentum and energy to other regions of the planet (Schubert 1983; Gierasch 1987; Schinder et al. 1990). Linear calculations indicate that ducted gravity waves in the stable layer generated from above by cloud-level convection have horizontal wavelengths of 30–50 km (Gierasch 1987), but more recent linear calculations of ducted gravity waves by Schinder et al. (1990) exhibit smaller horizontal wavelengths of roughly 10 km and intrinsic horizontal phase speeds of a few meters per second (relative to the convection layer). Finally, convection–wave interaction may help explain the large cellular features observed in cloud-top ultraviolet images. Cloud-level convection may deeply penetrate the underlying stable layer, generate internal gravity waves in the stable layer, and interact with convection in the lower atmosphere through convection–wave coupling. Such a process would form a deep convection–wave system with potentially large horizontal scales (Baker and Schubert 1992).

Thermal convection is a plausible wave generation mechanism in Venus's atmosphere (Schubert 1983; Schubert and Walterscheid 1984; Hou and Farrell 1987; Gierasch 1987; Schinder et al. 1990; Baker and Schubert 1992; Leroy 1994; Leroy and Ingersoll 1995, 1996). Pioneer Venus detected two neutrally stable regions in the atmosphere of Venus: one in the lower atmosphere from roughly 18- to 30-km altitude and the other in the middle cloud layer from roughly 48- to 55-km altitude (Seiff et al. 1980). In addition, a neutrally stable boundary layer likely exists adjacent to the surface (Seiff 1983; Young et al. 1987). These regions of neutral stability are probable sites of convection since convection tends to adjust the thermal structure toward neutral stratification. VEGA balloons, drifting at 54-km altitude within the cloud-level neutrally stable layer, found a strong positive correlation (85%) between vertical velocity and thermal perturbations, thus indicating that thermal convection occurs within the cloud layer (Ingersoll et al. 1987). Given the close proximity of convection to the stable layer from 30- to 48-km altitude, internal gravity waves within the stable layer may be forced by either cloud-level convection (Schubert 1983; Gierasch 1987; Seiff et al. 1992), lower atmosphere convection (Hou and Farrell 1987; Baker and Schubert 1992), or convection in both layers (Baker and Schubert 1992).

Convection models previously used to investigate convectively generated internal gravity waves in Venus's atmosphere suffer from many limitations. Studies that parameterize convective forcing of waves by diabetic heating with Gaussian (Schubert and Walterscheid 1984; Schinder et al. 1990) or delta function (Gierasch 1987) vertical distributions only consider thermal forcing of gravity waves and therefore neglect mechanical forcing by convective plumes. Mechanical forcing of internal gravity waves by deep cumulus convection has been shown to be an important wave generation mechanism in Earth's stratosphere (Fovell et al. 1992). Hou and Farrell (1987) employed simple periodic forcing as a proxy for convective plumes in Venus's atmosphere, but such forcing unrealistically assumes regular, nonturbulent behavior by atmospheric convection. Mixing length theory has also been used to convectively force internal gravity waves on Venus (Leroy 1994; Leroy and Ingersoll 1995, 1996). These studies incorporate both thermal and mechanical forcing mechanisms by convection and include a Kolmogorov turbulence spectrum with prescribed peak velocities of 3–5 m s^{-1}. However, the applicability of mixing length theory in Venus's atmosphere is questionable. Mixing length treatments assume that the convection layer is much smaller than a scale height. In Venus's atmosphere, both the lower convection layer and the cloud-level convection layer are comparable in thickness to the local pressure scale height [the scale height at 24-km altitude is $\sim$12 km and the scale height at 50-km altitude is $\sim$7 km (Schubert 1983)] and even thicker than the local pressure scale height if penetrative effects are included. Indeed, mixing length theory may underestimate vertical velocities on Venus by a factor of 3 or more (Baker et al. 1998).

Here, we present two-dimensional, nonlinear, fully compressible numerical simulations of convectively generated internal gravity waves in the lower atmosphere of Venus. The model overcomes many limitations exhibited by previous gravity wave studies by allowing for deep (multiple scale height) convection and by permitting convection to develop naturally (i.e., convective forcing is not prescribed a priori). The vertical domain extends from 12- to 60-km altitude, thus including both the lower convection region and the cloud-level convection layer. The gravity waves of interest occur in the stable layer from 30- to 48-km altitude, bounded above and below by convection layers. Characteristics of convectively generated internal gravity waves in the model are determined and compared with observations. A simulation without mean wind shear (i.e., without the Venus atmospheric superrotation) is presented; Part II of this study (Baker et al. 2000) presents results from a convectively generated gravity wave simulation with the Venus atmospheric superrotation. The next section introduces the mathematical model and numerical approach used to investigate convectively generated internal gravity waves. Section 3 presents a numerical simulation without mean wind shear. Implications of these results for Venus's atmosphere are presented in the discussion section.

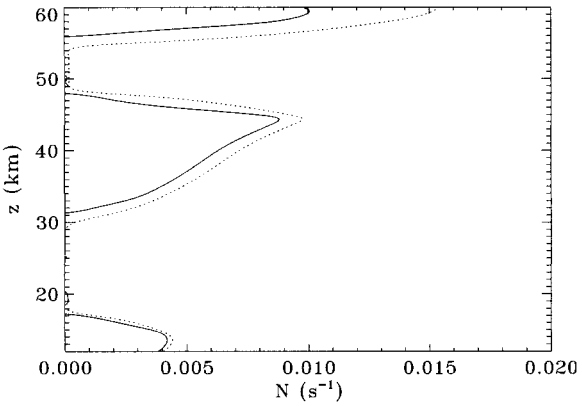

FIG. 1. Time-averaged, horizontally averaged Brunt–Väisälä frequency N as a function of altitude for the no mean wind shear case (solid). The background Brunt–Väisälä frequency (dotted) is also shown. Convection layers exist where $N \sim 0$, and stable layers occur where $N > 0$.

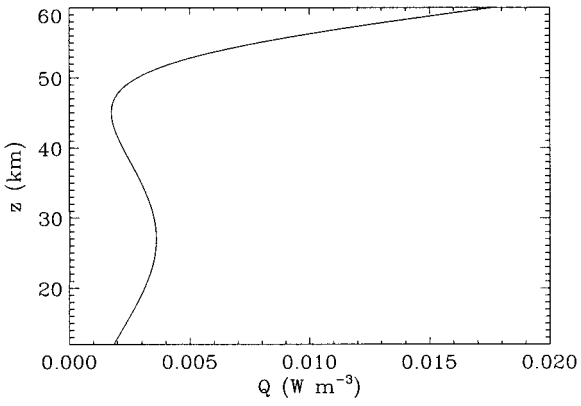

FIG. 2. Model subsolar heating Q as a function of altitude z.

2. Model

The mathematical model of Venus's atmosphere and the numerical approach are fully described in Baker et al. (1998, 1999). Briefly, we use a 2D, nonlinear, fully compressible model of a perfect gas to simulate Venus atmospheric convection and gravity wave generation from 12- to 60-km altitude. Full compressibility is required because convection in Venus's atmosphere spans a scale height or more and local compressibility preferentially produces strong, narrow downwellings (Hurlburt et al. 1984). Variables in our model such as density, velocity, and potential temperature are decomposed into two components: a steady (at the timescales of our simulations) background state that is supported by processes such as thermal radiation, large-scale dynamics, and small-scale eddies (eddy diffusion) with timescales much longer than convection and waves, and time-dependent deviations from this background state that include convection and waves with timescales of seconds to hours. A Venus-like background thermal structure similar to that used by Young et al. (1987) is adopted (Fig. 1). Time-dependent deviations (convection and gravity waves) are driven by absorption of solar radiation in the clouds. The simulations in this paper consider solar heating at the subsolar point (Fig. 2), the maximum solar heating possible in Venus's atmosphere. Subsolar heating is determined from extrapolation of Pioneer Venus solar flux measurements (Tomasko et al. 1980). Small-scale turbulence is modeled by eddy diffusion with constant diffusion coefficients. The conservation equations of mass, momentum, and energy are solved explicitly using a time-adaptive leapfrog scheme for all but the diffusion terms, which are solved using an implicit Crank–Nicolson scheme and Jacobi iteration in the energy equation and an explicit time-lag scheme in the momentum equations. Spatial derivatives are computed using centered, second-order differences on a vertically staggered grid. A frequency filter (Asselin 1972) is applied at every time step to dampen the leapfrog computational mode.

Table 1 lists the dimensional and nondimensional Venus parameter values used in the model simulation, where g is the acceleration of gravity, R is the gas constant, c_p is the specific heat at constant pressure, κ_m is the eddy momentum diffusivity, κ_θ is the eddy thermal diffusivity, d is the total depth, ρ_0 is the reference density, T_0 is the reference temperature, and q_0 is the reference volumetric solar heating. The reference level is at 60-km altitude. The value of c_p used in this model is appropriate for a temperature of 445 K (Staley 1970), the mean temperature at roughly 36-km altitude. The companion paper (Baker et al. 2000) presents results of a simulation with the same parameter values except that the Venus westward superrotation is included.

Since Venus's atmosphere is radiatively opaque below 60-km altitude, longwave radiation can be modeled by a radiative diffusivity (Hou and Goody 1989). The value of eddy diffusivity used in our calculations (discussed in more detail below) is larger than the radiative diffusivity at all altitudes (the radiative diffusivity has a minimum value of ~ 0.1 m^2 s^{-1} at 12-km altitude and

TABLE 1. Model parameter values for the Venus gravity wave simulation.

Parameter	Value	Nondimensional parameter	Value
g	8.87 m s^{-2}		
R	191.4 J kg^{-1} K^{-1}	σ	1.00
c_p	970 J kg^{-1} K^{-1}	γ	1.25
κ_m	155 m^2 s^{-1}	C_g	8.30
κ_θ	155 m^2 s^{-1}	C_k	1.43×10^{-5}
d	48.0 km	C_q	3.35×10^{-5}
ρ_0	0.4291 kg m^{-3}	$Ra\dagger_q$[a]	6.8×10^{6}[b]
T_0	268 K		1.2×10^{6}[c]
q_0	1.76×10^{-2} W m^{-3}		

[a] The convection layer depth is used rather than the total depth in determining the Rayleigh number.
[b] The cloud-level convection layer Rayleigh number.
[c] The lower convection layer Rayleigh number.

a maximum value of ~40 $m^2\ s^{-1}$ at 60-km altitude). We do not explicitly include radiative diffusivity in our model, although eddy diffusivity could be interpreted to represent both turbulent and radiative effects. Regardless, Venus's atmosphere is dominated by convective and diffusive processes below 60-km altitude. Absorption of solar radiation is the primary forcing mechanism for these convective and diffusive processes. Because solar heating is strongest at the top of the domain (Fig. 2), one may initially conclude that absorption of solar radiation provides a stabilizing influence in Venus's atmosphere. However, the Venus profile of solar heating actually provides a destabilizing influence on the atmosphere (Baker et al. 1999). Since the atmosphere behaves diffusively below 60-km altitude, negative potential temperature gradients are established to transfer the absorbed solar radiation. Larger values of solar heating result in steeper (more negative) potential temperature gradients, and convectively unstable regions are produced. The situation is somewhat analogous to a uniformly internally heated system in which convection occurs even though heating is uniformly distributed. It is important to note here that the thermal boundary conditions at 12-km altitude and 60-km altitude in our model consist of fixed eddy diffusion heat flux conditions. The value of eddy diffusion heat flux at the boundaries is equal to (but opposite in sign from) the solar heat flux at that altitude. Since eddy diffusivity in our model may be partially viewed as parameterizing longwave radiation, the fixed heat flux boundary conditions partially account for longwave radiative heating at the lower boundary and for longwave radiative cooling near the cloud tops.

The value of eddy diffusivity used in the model (155 $m^2\ s^{-1}$) is comparable to recent estimates (120–150 $m^2\ s^{-1}$) from radio scintillation data on scales less than 1 km (Leroy 1994). Currently, these estimates of eddy diffusivity are the only available estimates for diffusion by small-scale turbulent eddies in Venus's atmosphere with spatial scales $\leq$1 km. For mixing lengths larger than 1 km, the range of eddy diffusivity is much broader, with estimates from photochemical modeling of roughly 2 $m^2\ s^{-1}$ (Krasnopolsky and Parshev 1981, 1983; Krasnopolsky 1985; Yung and Demore 1982) and estimates from Galileo and Vega balloon observations of 60–1500 $m^2\ s^{-1}$ (James et al. 1997). However, ''large-scale'' eddy diffusivity parameterizes convective motions explicitly resolved in our model, and one therefore should not expect large-scale eddy diffusivities to match ''small-scale'' eddy diffusivities in value. We consider the value of eddy diffusivity used in the model to be an upper bound for diffusion by small-scale turbulent eddies. Computational considerations currently limit the use of lower values of eddy diffusivity. Nevertheless, lower values of eddy diffusivity will likely result in stronger convective penetration and entrainment (Baker et al. 1999). The implications of sensitivity to eddy diffusivity are presented in the discussion section.

When the nonlinear, fully compressible equations are scaled by d, ρ_0, T_0, q_0, and the reference sound crossing time $d/(RT_0)^{1/2}$, the following nondimensional parameters result:

$$\sigma = \frac{\kappa_m}{\kappa_\theta}, \tag{1}$$

$$\gamma = \frac{c_p}{c_v}, \tag{2}$$

$$C_g = \frac{dg}{RT_0}, \tag{3}$$

$$C_k = \frac{\kappa_\theta}{d(RT_0)^{1/2}}, \tag{4}$$

$$C_q = \frac{dq_0}{\rho_0 c_p T_0 (RT_0)^{1/2}}, \tag{5}$$

where c_v is the specific heat at constant volume. The Prandtl number σ represents the relative strength of momentum diffusion compared with heat diffusion, and γ determines the density change during adiabatic pressure fluctuations. The parameter C_g may be interpreted as the ratio of the time for a sound wave to travel a distance d (the sound crossing time) to the free-fall time through a layer with depth d, or alternatively, as the ratio of the depth of the layer to the isothermal scale height at the reference level. The quantity C_k is the ratio of the sound crossing time to the thermal diffusion time, and C_q is the ratio of the sound crossing time to the characteristic heating time.

An additional nondimensional parameter, the internally heated Rayleigh number Ra_q, can be expressed as a combination of the nondimensional compressible parameters given in Eqs. (1)–(5):

$$\mathrm{Ra}_q = \frac{gq_0 d^5}{T_0 \rho_0 c_p \kappa_\theta^2 \kappa_m} = \frac{C_g C_q}{\sigma C_k^3}. \tag{6}$$

The Rayleigh number, as a measure of the degree of thermal instability in a fluid, remains the most important parameter in characterizing thermal convection. It represents the relative efficiency of buoyancy forces due to internal heat generation in overcoming viscous forces due to small-scale turbulence. The Rayleigh number defined by Eq. (6), however, uses the total depth d of the layer and thus overestimates the convective instability in Venus's atmosphere. Instead, we chose the convection layer depth $d^\dagger$ to define an effective Rayleigh number $\mathrm{Ra}_q^\dagger$. Likewise, the reference level is taken to be at the top of the convection layer (where solar heating is greatest within the convection layer) rather than at 60-km altitude in calculating $\mathrm{Ra}_q^\dagger$. The convection layer depth $d^\dagger$ and the reference level are determined a posteriori since convective penetration and entrainment widen the convection layer from its background state thickness (Fig. 1). The values of $\mathrm{Ra}_q^\dagger$ for the lower convection

layer and for the cloud-level convection layer are 1.2×10^6 and 6.8×10^6, respectively.

The computational domain extends 120 km horizontally and spans vertically from 12- to 60-km altitude. The lower boundary is placed at 12-km altitude for two reasons: 1) reliable data from the Pioneer Venus probes only extend down to 12-km altitude, and 2) inclusion of the additional scale height of atmosphere from the surface to 12-km altitude would impose additional computational burden. A grid of 650×403 points is used with a horizontal grid spacing of $\sim$0.18 km and a vertical grid spacing of $\sim$0.12 km. Such high resolution is needed to resolve extremely narrow convective downdrafts and nonlinear wave generation by convective penetration (Baker et al. 1998). Since the fully compressible model includes sound waves, a small time step of approximately 0.10 s is required to meet the Courant condition for stability.

The horizontal boundaries are stress free with a fixed heat flux, and the side boundaries are periodic. Impermeable, stress-free boundaries cause artificial wave reflection and an intensification of gravity wave amplitudes in the stable layers adjacent to the boundaries (from 12- to 18-km altitude and from 56- to 60-km altitude). However, as shown in Baker et al. (1998), artificially trapped gravity waves do not significantly alter the convection, and therefore impermeable, stress-free boundaries should not influence the convectively generated gravity waves in the stable layer from 30- to 48-km altitude. The value of eddy diffusion heat flux at the boundaries is equal to but opposite in sign from the solar flux at that level.

The initial condition is a lower Rayleigh number (higher eddy diffusivity) solution that ultimately developed from small thermal perturbations ($\leq$1%) against a motionless, conductive state. A short transient phase occurs as the simulation adjusts from the initial condition to a statistically steady state. The statistically steady integration time is 32.4 h.

3. Results

Two convection regions in Venus's atmosphere are simulated: the lower atmosphere convection layer from roughly 17- to 31-km altitude and the cloud-level convection layer from roughly 47- to 56-km altitude (Fig. 3). A stable layer exists between the two convection layers; this stable region supports internal gravity waves. In addition, stable layers exist below the lower convection layer and above the cloud-level convection layer. Transition regions occur between a convection layer and adjacent stable layers. As described below, convection in both convection layers is characterized by cold downdrafts that penetrate underlying stable regions. We therefore describe transition regions *below* convection layers as penetrative regions. Similarly, downdrafts near the top of the convection layers entrain overlying stable air into the convective regions. We

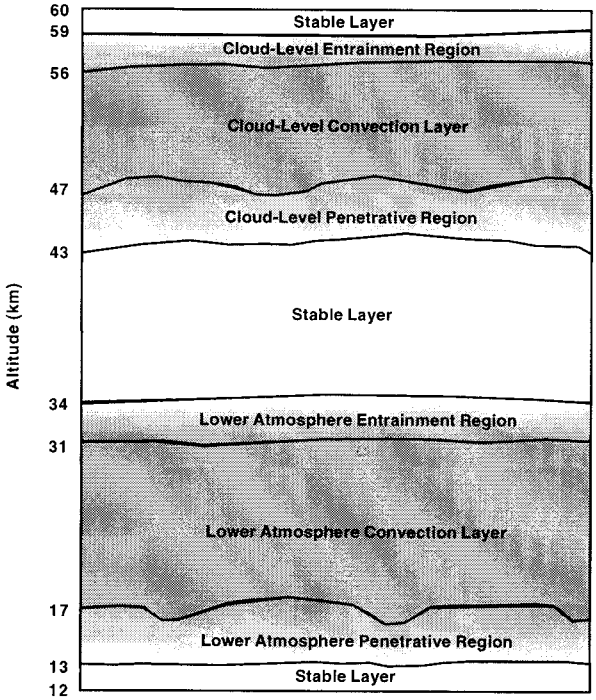

FIG. 3. Schematic of the layered dynamic structure in Venus's atmosphere.

therefore label transition regions located *above* convection layers as entrainment regions. Dynamical characteristics of the convection layers, transition regions, and the middle stable layer are described below.

a. Convection characteristics

Figure 4 shows residual potential temperature θ'' (total potential temperature minus the horizontally averaged potential temperature) and velocity field for the case without mean wind shear at one instant in time, where x is horizontal distance, z is altitude, and t is the simulation time. Characteristics of the cloud-level convection layer are similar to results presented in Baker et al. (1998, 1999). Cloud-level convection is distinguished by cold, narrow downwellings that deeply penetrate the underlying stable layer. The horizontal widths of cloud-level convective downdrafts are 1–2 km with horizontal spacings of 15–30 km. As a convective downdraft penetrates the underlying stable layer, stable air splashes upward into the convection layer along with a portion of the downwelling plume head (e.g., colder, stable air is forced into the convection layer by the strong downdraft at $x = 67$ km, $z = 46$ km). The remaining portion of the downwelling plume head undergoes strong compressional heating with potential temperatures within the compressional features up to 4 K warmer than the environment. Downdrafts in the cloud-level convection layer have typical downward velocities of $\sim$5–7 m s^{-1} at 54-km altitude and stronger

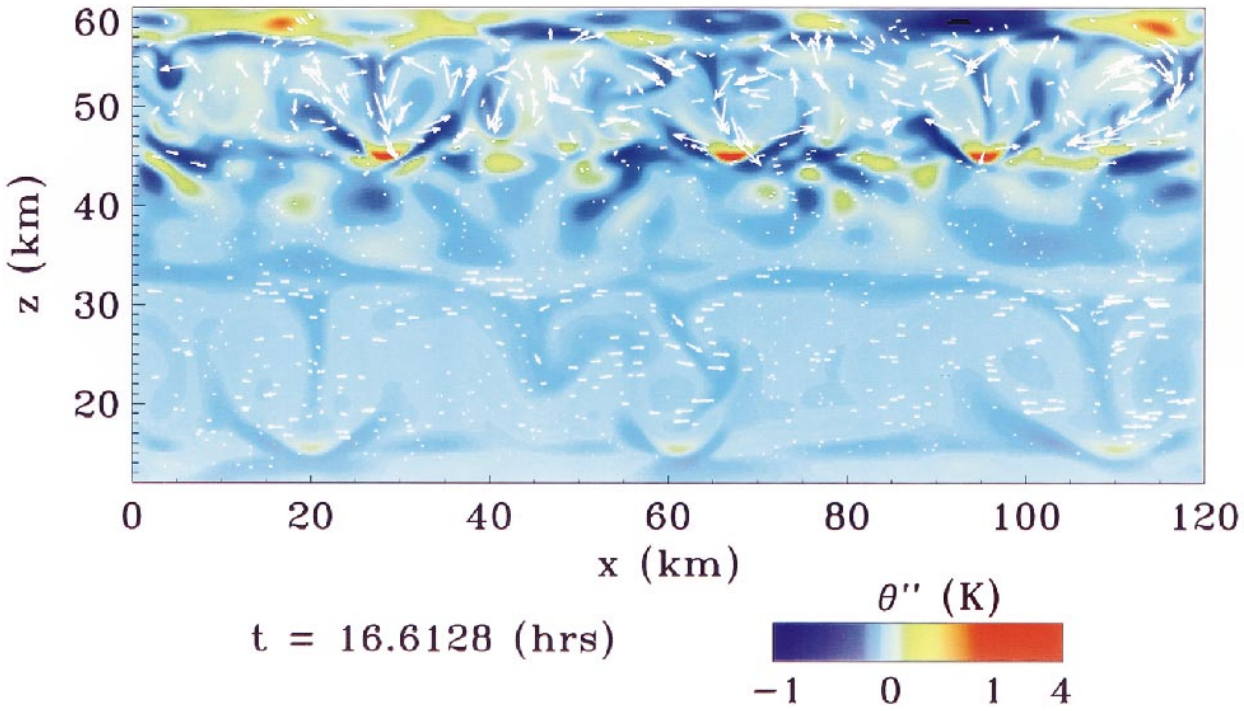

FIG. 4. Residual potential temperature θ'' (colors) and velocity field (arrows) at one instant in time. The lower convection layer spans from 17- to 31-km altitude, and the cloud-level convection layer extends from 47- to 56-km altitude. Stable layers occur from 12- to 17-km, 31- to 47-km, and 56- to 60-km altitude. The longest arrow represents a velocity of 13.3 m s^{-1}.

downward velocities of ~9–13 m s^{-1} as they penetrate the underlying stable layer at 47-km altitude. Upward velocities are somewhat smaller (the upflow regions are distinctly broader) with typical values of 4–6 m s^{-1} throughout the layer. Downward convective penetration generates internal gravity waves in the underlying stable layer with potential temperature amplitudes of roughly 0.5 K and horizontal wavelengths of roughly 10–15 km. Characteristics of internal gravity waves in the stable layer from 31- to 47-km altitude will be discussed in more detail below.

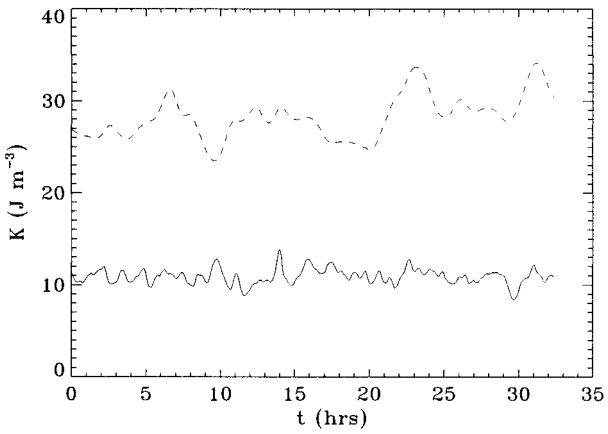

FIG. 5. Spatially averaged kinetic energy density for the cloud-level convection layer (solid) and the lower convection layer (dashed) as a function of time.

Convection in the lower atmosphere is also characterized by cold, narrow downwellings (Fig. 4). Downdraft widths in the lower convection layer are 2–3 km and the horizontal spacing between downdrafts is 15–50 km. Again, downward convective penetration is present, but upward mechanical forcing and compressional heating of plume heads is less intense than for cloud-level convection because lower-atmosphere convection is less vigorous. Typical downward velocities near the top of the convection layer (30-km altitude) are 1–2 m s^{-1}. Near the bottom of the convection layer at 18-km altitude, downward velocities are larger (3–5 m s^{-1}). Upward vertical velocities, with typical values of 2–3 m s^{-1}, are only slightly smaller than downward vertical velocities.

The thickness of both the lower convection layer and the cloud-level convection layer is modified by convective penetration and entrainment (Fig. 1). The lower-atmosphere convection layer is thicker than the background neutrally stable region by roughly 2 km because downward penetration into the underlying stable layer and convective entrainment of the overlying stable layer partially erode adjacent stable regions. Similarly, the thickness of the cloud-level convection layer is slightly larger than the thickness of the cloud-level background neutrally stable layer. The stable layer between the two

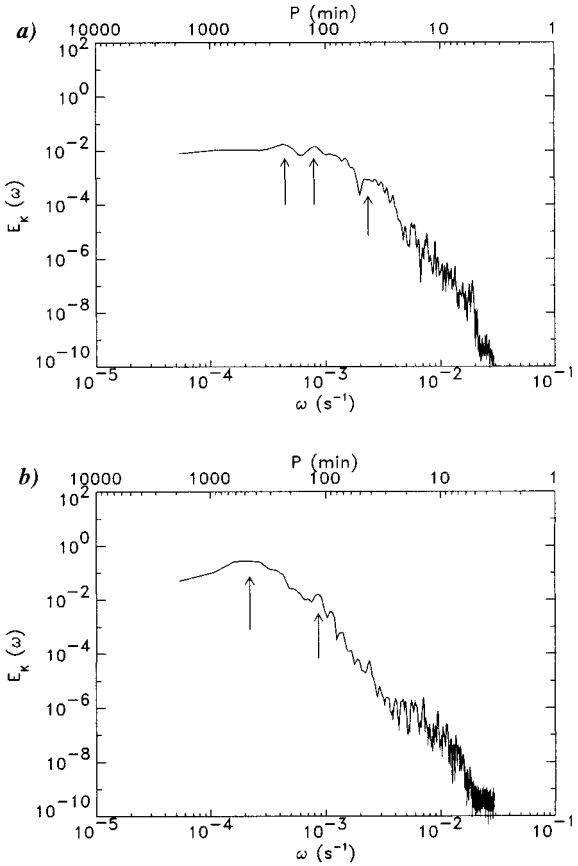

FIG. 6. Power spectral density E_K of spatially averaged kinetic energy density K as a function of angular frequency ω and period P for the cloud-level convection layer (top) and the lower atmosphere convection layer (bottom). Arrows indicate dominant peaks discussed in the text. The units of E_K are $J^2\ m^6\ s^{-1}$.

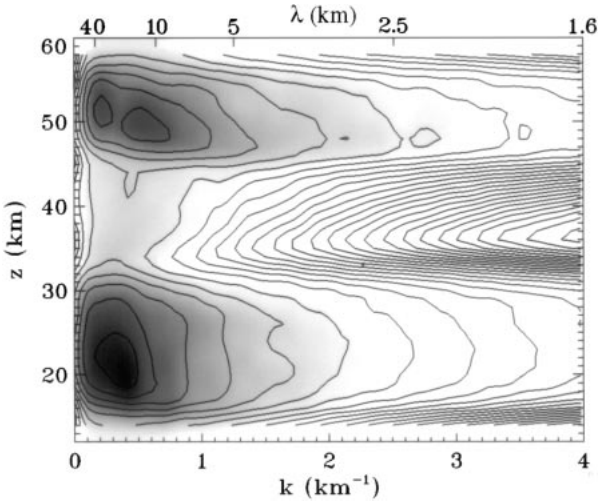

FIG. 7. Time-averaged power spectral density of $\rho^{1/2}w'$ as a function of horizontal wavenumber k (or horizontal wavelength λ) and altitude z. Contours represent the logarithm of power spectral density with an interval of 0.5. Dark shading depicts regions of large power.

convection regions is correspondingly reduced in vertical extent by ~2 km.

Figure 5 is a plot of the time series of the spatially averaged kinetic energy density K within both convection layers. Only the convectively active portion of the domain (14–34-km altitude for lower-atmosphere convection and 43–58-km altitude for cloud-level convection, including penetrative effects) is considered in calculating K. Even though velocities are smaller by a factor of 2 or 3 in the lower convection layer than in the cloud-level convection layer, K in the lower convection layer is larger because the average density in the lower convection layer is an order of magnitude larger than in the cloud layer. Both convection layers exhibit time-dependent behavior. Spectral analysis of the kinetic energy density time series indicates dominant periods of approximately 8 and 2 h in the lower convection layer (Fig. 6). The 8-h oscillation is associated with the convective overturning time, and the 2-h cycle is associated with the lifetime of compressional features due to penetrative convection. Higher frequency oscillations occur in the cloud-level convection layer, with dominant periods of roughly 4 h, 2 h, and 45 min. The characteristic overturning time in the cloud-level convection layer is roughly 2 h with a characteristic penetrative timescale of roughly 45 min, consistent with results from the cloud-level 100% subsolar heating case presented in Baker et al. (1998). The longer period fluctuation of roughly 4 h is a modulation of kinetic energy by strong convective downdrafts. Occasionally, weaker downwellings merge into strong downdrafts; these strong downdrafts form every few convective overturns.

As Fig. 4 shows, the horizontal scale of convection is slightly larger in the lower convection layer than in the cloud-level convection layer. This idea is further reinforced by spectral analysis of $\rho^{1/2}w'$ (Fig. 7), where ρ is density and w' is the vertical velocity deviation from the background state. Vertical velocity fluctuations are weighted by $\rho^{1/2}$ to account for the exponential dependence of density with altitude. With this scaling, the spectral power density of $\rho^{1/2}w'$ represents (within a factor of two) the deviation kinetic energy density per unit wavenumber. Spectra as a function of horizontal wavenumber k are taken at each altitude level at time intervals of roughly 75 min from $t = 16.6$ h to $t = 32.4$ h. The spectra are then averaged in time, and the results are plotted in Fig. 7. At all altitudes, significant power resides at horizontal wavenumbers smaller than the Nyquist wavenumber ($k = 17.4\ km^{-1}$). Cloud-level convection exhibits horizontal wavelengths of ~30 km in the middle of the layer with smaller-scale features (wavelengths of ~9–15 km) evident in the lower part of the layer. The smaller-scale features are associated with ''splashed'' plume heads and stable air from below (e.g., small-scale features can be seen in Fig. 4 near the strong downdraft at $x = 67$ km, $z = 46$ km). Even smaller-scale features are present near the convection–

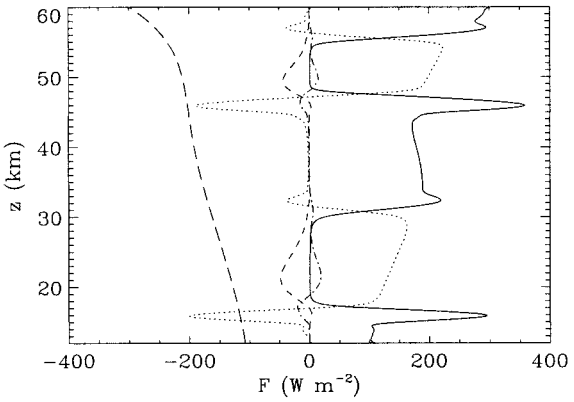

FIG. 8. Time-averaged heat fluxes as a function of altitude. Plotted are the convective heat flux F_c (dot), eddy diffusion heat flux F_e (solid), kinetic energy flux F_k (dash), pressure energy flux F_p (dash–dot), and solar heat flux F_q (long dash).

stable layer interface at roughly 47-km altitude, indicative of small-scale mixing near the penetrative region. In comparison, convection in the lower atmosphere shows dominant wavelengths of roughly 20–30 km throughout the layer. A slight tendency toward higher wavenumber (smaller wavelength) can be seen at 18-km altitude, but the length scales are still considerably larger than those found in the cloud-level penetrative region. A broad spectrum of internal gravity waves with horizontal wavelengths of roughly 7–40 km is generated in the stable layer between the two convection regions, with the largest power at wavelengths of ~10–15 km. Larger wavenumber (shorter wavelength) features are absent in the stable layer because wave forcing by convection at large wavenumbers is weak.

The partitioning of heat transfer in our model is controlled by convective, diffusive, kinetic, pressure, and solar heating terms. The convective heat flux F_c, eddy diffusion heat flux F_e, kinetic energy flux F_k, energy flux associated with pressure fluctuations F_p, and solar heat flux F_q are defined as

$$F_c = \langle \rho c_p \theta'' w' \rangle, \tag{7}$$

$$F_e = -\left\langle \rho c_p \kappa_\theta \frac{d\theta'}{dz} \right\rangle, \tag{8}$$

$$F_k = \frac{1}{2} \langle \rho u_i' u_i' w' \rangle, \tag{9}$$

$$F_p = \langle p'' w' \rangle, \tag{10}$$

$$F_q = \langle F_Q' \rangle, \tag{11}$$

where the angle brackets indicate a horizontal average, a prime indicates deviations from the background state, a double prime indicates residuals from the horizontal average, ρ is density, θ is potential temperature, w is the vertical velocity, u_i is the velocity in the x_i direction, p is pressure, and F_Q is the vertical integral of volumetric solar heating Q shown in Fig. 2. We use the convention that upward energy or heat transfer is positive.

Figure 8 shows time-averaged heat fluxes from 12- to 60-km altitude. Within the convection layers, solar heat flux is largely balanced by convective heat flux. Positive values of F_c indicate that vertical velocity and potential temperature fluctuations are positively correlated and heat transfer by convection is upward. Negative values of F_c indicate regions of convective penetration or entrainment in which relatively warm air (positive θ'') is forced downward by convective downdrafts (negative w'). Average downward penetration by cloud-level convection extends from the bottom of the convection layer at 47-km altitude to roughly 43-km altitude. Similarly, lower-atmosphere convection penetrates roughly 4 km into the underlying stable layer to roughly 13-km altitude. The lower boundary at 12-km altitude, however, may limit the extent of penetration by the lower convection layer; downward penetration could be even greater if the lower boundary occurred closer to the surface. For both convection layers, the amount of heat transferred downward by convective plumes within the penetrative regions is comparable to the solar heat flux at the respective altitudes.

Negative values of F_c located above the convection layers are the result of convective entrainment by strong downdrafts. Convective entrainment has been shown to be a potentially important mechanism for convection layer growth in Venus's atmosphere (Baker et al. 1999). Here, entrainment by convective downdrafts in the lower convection layer and in the cloud-level convection layer occurs up to altitudes of 34 and 59 km, respectively. The upper boundary at 60-km altitude may limit the thickness of the entrainment region above the cloud-level convection layer. The amount of heat transferred downward by entrainment is significantly smaller than that transferred by convective penetration into underlying stable layers, largely because convective velocities are reduced near the top of the convection layers.

The kinetic energy flux F_k is directed downward throughout the convection layers because convection is characterized by cold, narrow downwellings in which most of the kinetic energy of the system resides; F_k is largest in magnitude near the bottom of the convection layers where densities are largest and downdrafts achieve their highest velocities. Moreover, the pressure energy flux F_p is positive within the convection layers. Pressure fluctuations near the bottom of a convection layer help drive diffuse upflows in compressible convection (Hurlburt et al. 1984); thus, relatively large values of F_p occur in the lower portion of the convection layers. These positive values of F_p help offset the strong negative kinetic energy flux in the lower portion of the convection layers. In the penetrative regions, F_p is negative due to compressional regions (high p'') associated with downflow plume heads.

Finally, the eddy diffusion heat flux F_e is negligible within the convection layers since the convection layers

exhibit a nearly adiabatic interior (Fig. 1). However, F_e is the dominant mode of heat transfer (along with solar heating) within the stable layers (Fig. 8). The eddy diffusion heat flux is also quite large in the penetrative regions, indicating that convective penetration generates significant small-scale turbulence. These results are largely insensitive to the value of eddy diffusivity. With a different value of eddy diffusivity, the temperature gradient would adjust such that the eddy diffusion heat flux would balance the solar heat flux in the stable layers (i.e., the value of F_e would not change). However, a different value of eddy diffusivity does produce variation in convective penetration and entrainment, which can alter the mean thermal structure in the penetrative and entrainment regions (Baker et al. 1999).

b. Gravity waves

1) CHARACTERISTICS

Wave motions in the simulation without mean wind shear exist in the stable layer from 31- to 47-km altitude. As we show in this section, these wave motions are internal gravity waves generated primarily by cloud-level penetrative convection. Intrinsic horizontal phase speeds of internal gravity waves (discussed in more detail below) are comparable to convective velocities in the cloud layer, and horizontal wavelengths (7–40 km with a dominant wavelength of ~15 km) are similar in scale to cloud-level convection (Fig. 7). Cloud-level convection and gravity wave propagation operate on much faster timescales than atmospheric dynamics below 34-km altitude. Indeed, animation of the residual potential temperature field shows the atmosphere above roughly 34-km altitude to be largely decoupled from the atmosphere below. Gravity waves rapidly propagate away from penetrating plume heads in both horizontal directions, although some vertical propagation does occur (note the tilted phase lines of potential temperature (lines of constant color in the image) within the stable layer in Fig. 4). Vertical wave propagation, however, is limited by the lower convection layer; convectively generated internal gravity waves are vertically trapped from roughly 31- to 47-km altitude.

To show that simulated wave motions in the stable layer are indeed internal gravity waves, we plot coherence, cross-spectrum amplitude, and phase of vertical velocity and potential temperature time series taken at $x = 60$ km, $z = 39$ km (Fig. 9). Coherence measures the frequency correlation between w' and θ''; if both time series experience oscillations at a given frequency, then coherence at that frequency will be high. The maximum possible value of coherence is 1.0. The cross-spectrum amplitude is a measure of the spectral power in both signals. Small cross-spectrum amplitudes indicate that coherence and phase spectra are unreliable; that is, oscillations may be present at a given frequency but the amplitudes are negligible. The phase can be interpreted as the phase difference between the two time series at a given frequency. For linear internal gravity waves, w' and θ'' are 90° out of phase (Stull 1988). At 39-km altitude (the middle of the stable layer), coherence between vertical velocity and potential temperature fluctuations is rather high for nearly all frequencies, especially for frequencies near the Brunt–Väisälä frequency N. Gravity waves in an isothermal atmosphere have frequencies less than or equal to the Brunt–Väisälä

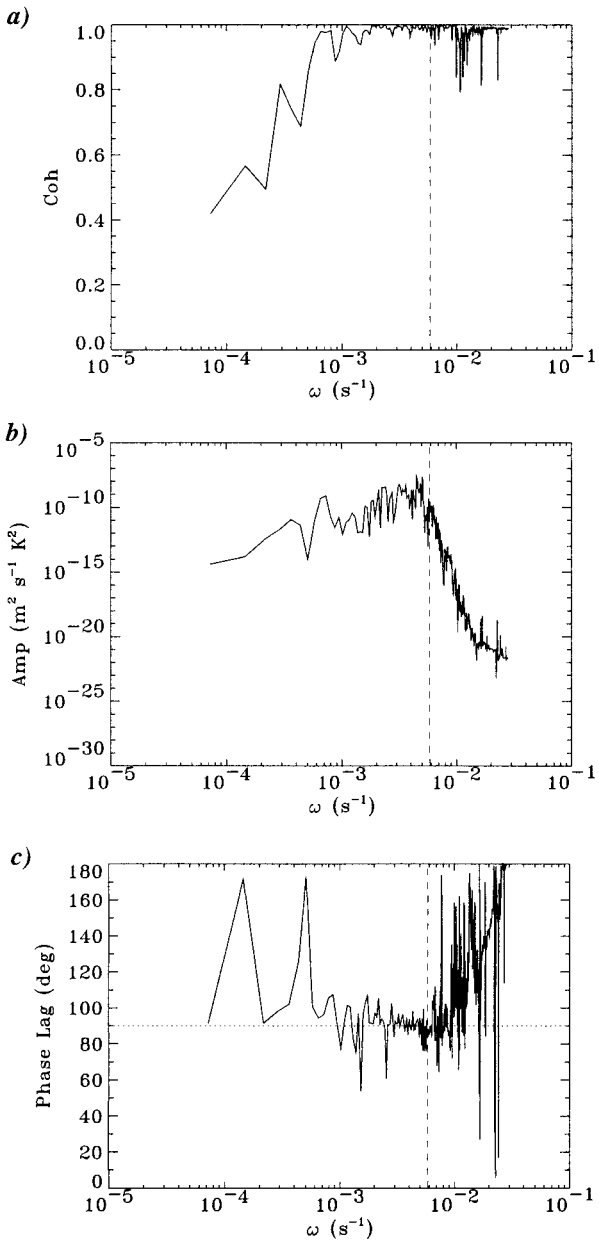

FIG. 9. Coherence (top), cross-spectrum amplitude (middle), and phase (bottom) of w' and θ'' at 39-km altitude and $x = 60$ km as a function of angular frequency ω. The dashed line is the time-averaged, horizontally averaged Brunt–Väisälä frequency at 39-km altitude. The dotted line in the phase plot marks a phase difference of 90°.

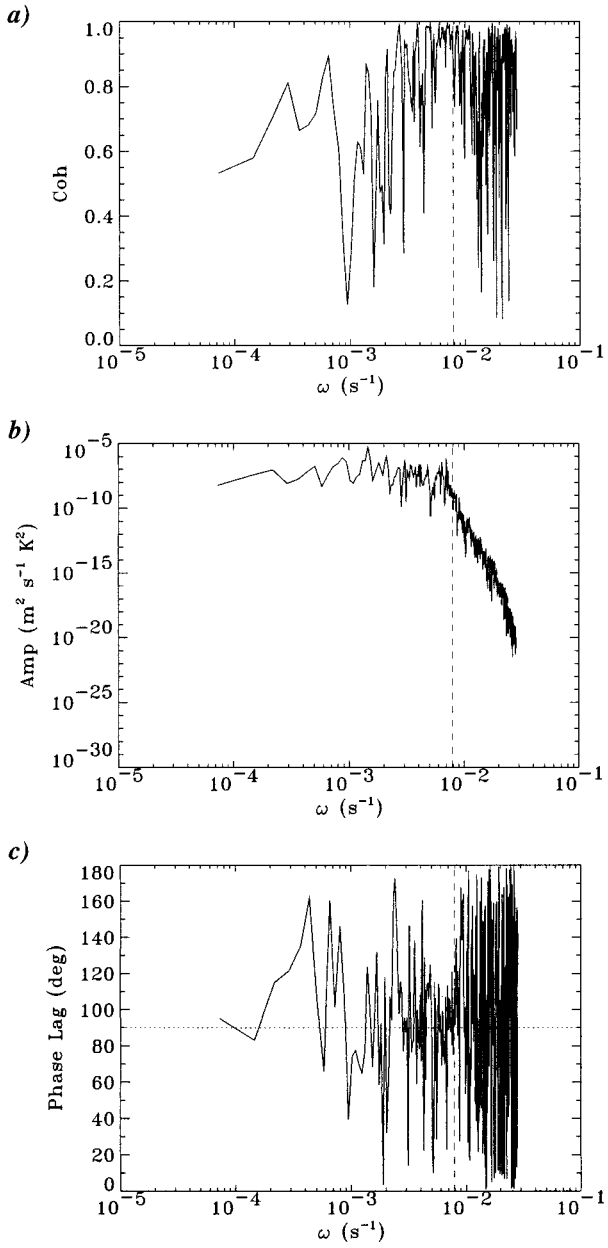

FIG. 10. Coherence (top), cross-spectrum amplitude (middle), and phase (bottom) of w' and θ'' at 45-km altitude and $x = 60$ km as a function of angular frequency ω. The dashed line is the time-averaged, horizontally averaged Brunt–Väisälä frequency at 45-km altitude. The dotted line in the phase plot marks a phase difference of 90°.

frequency (Beer 1974). The cross-spectrum amplitude indicates that both w' and θ'' experience relatively large power at frequencies less than N. Furthermore, vertical velocity and potential temperature are roughly 90° out of phase for $\omega \leq N$. Thus, vertical velocity and potential temperature oscillations show significant power at frequencies less than the Brunt–Väisälä frequency and exhibit a 90° phase lag, both properties characteristic of linear internal gravity waves.

The situation is more complex in the cloud-level penetrative region. Figure 10 shows coherence, cross-spectrum amplitude, and phase of vertical velocity and potential temperature fluctuations taken at the horizontal midpoint ($x = 60$ km) at 45-km altitude. Again, most of the combined power of w' and θ'' occurs at frequencies less than N, but coherence shows a broader range (0.2–1.0) than in the stable layer. In addition, the phase shift between w' and θ'' departs significantly from 90° at frequencies with the highest cross-spectrum amplitude. In other words, the time series of w' and θ'' in the penetrative region exhibit strong nonlinear signatures that overwhelm any linear gravity wave signal that may be present. The nonlinear motions have previously been described as ''interfacial waves'' near the convection–stable layer interface (Baker et al. 1998).

The analysis of time series taken at a single point is less meaningful in a convection layer than in a penetrative region or in a stable layer because such an analysis is unlikely to capture the average conditions of the convective system. For example, the sample point may be located within a plume at all times. Time series taken at this sample location would distinctly capture plume dynamics. This would be a useful analysis, but the plume location cannot be determined a priori due to the time-dependent nature of convection. In other situations, the sample point may stay within the convection cell core at all times, and time series would represent atmospheric dynamics *away* from plumes. Indeed, a sample point in the convection layer may (or may not) encounter a variety of dynamical processes and thus likely will not be representative of the convection layer as a whole. Nevertheless, for completeness, Fig. 11 shows coherence, cross-spectrum amplitude, and phase of w' and θ'' in the cloud-level convection layer at ($x = 60$ km, $z = 51$ km). Nonturbulent time-dependent convection should exhibit strong coherence and large cross-spectrum amplitude with zero phase lag for a few dominant frequencies. This type of behavior does not appear in the vertical velocity and potential temperature signals in the middle of the cloud-level convection layer. Instead, most of the cross-spectrum amplitude occurs at low frequency where coherence is relatively low and phase oscillates dramatically. There is one frequency ($\omega = 8.8 \times 10^{-4}$ s^{-1} or a period of 120 min) with large amplitude, relatively high coherence of 0.77, and zero phase that may reflect convective overturning (see Fig. 5). However, the complex temporal signature of vertical velocity and potential temperature in the cloud-level convection layer suggests a departure from simple time-dependent behavior.

The difference in spatial and temporal scales between lower atmosphere convection, gravity waves in the stable layer, and cloud-level convection can be further confirmed by 2D Fourier analysis. Figure 12 shows the 2D power spectral density of $\rho^{1/2}w'$ as a function of ω and k in the lower convection layer (24-km altitude), the lower entrainment region (33-km altitude), the stable

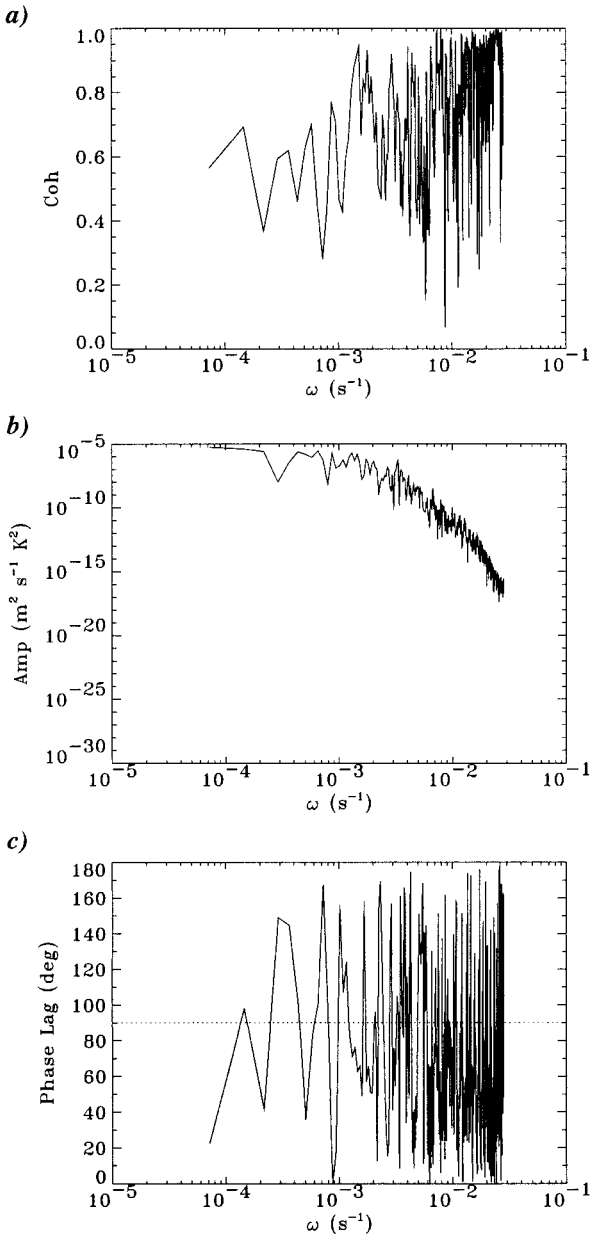

FIG. 11. Coherence (top), cross-spectrum amplitude (middle), and phase (bottom) of w' and θ'' at 51-km altitude and $x = 60$ km as a function of angular frequency ω. The dotted line in the phase plot marks a phase difference of 90°.

layer (39-km altitude), the cloud-level penetrative region (45-km altitude), and the cloud-level convection layer (51-km altitude). The density-weighted vertical velocity was sampled every 100 s at each horizontal grid point at a given altitude from $t = 24.1$ h to $t = 32.4$ h. Because data were sampled at every horizontal location, 2D spectral analysis better captures the temporal nature of the convection layers than does sampling from a single location. Both lower-atmosphere convection (Fig. 12e) and the lower entrainment region (Fig. 12d) are characterized by small wavenumbers (long horizontal wavelengths) and low frequencies (long periods). Gravity waves in the stable layer exhibit comparable wavelengths but higher frequencies than lower atmosphere convection and entrainment (Fig. 12c). The maximum 2D power spectral energy of $\rho^{1/2}w'$ at 39-km altitude occurs at $\omega = 4.8 \times 10^{-3}$ s^{-1} (22-min period) and $k = 0.52$ km^{-1} (horizontal wavelength of 12 km). The cloud-level penetrative region shows power distributed over a broader range of frequencies and wavenumbers (Fig. 12b). Both higher wavenumber and higher frequency features are seen in the penetrative region, indicative of rapid, smaller-scale mixing. The largest 2D spectral power at 45-km altitude, however, resides at the same frequency and wavenumber as the dominant gravity wave mode in the stable layer. This strongly suggests that the linear gravity wave signal found in the underlying stable layer is generated by cloud-level penetrative convection (animation of residual potential temperature confirms cloud-level wave generation). Finally, cloud-level convection exhibits largest spectral power at low wavenumber and low frequency, but also experiences significant power at smaller wavelengths and higher frequencies (Fig. 12a). Obviously, cloud-level convection operates on shorter length scales and timescales than lower-atmosphere convection and therefore is responsible for generation of rapidly fluctuating small-scale internal gravity waves. The forcing of gravity waves by convection occurs in the cloud-level penetrative region, as evidenced by the lack of a local maximum at $\omega = 4.8 \times 10^{-3}$ s^{-1} and $k = 0.52$ km^{-1} in Fig. 12a. Wave generation is directly tied to the penetrative region (rather than to the convection layer), and thus the penetrative region can be considered a transition zone from a convective response to a gravity wave response.

Figure 13 plots the spectral energy density of $\rho^{1/2}w'$ at horizontal position $x = 60$ km as a function of angular frequency ω and altitude. The earlier comments regarding time series analysis from a single location within convection layers also apply here. In the stable layer, however, time series of $\rho^{1/2}w'$ sampled from a single point will capture propagating gravity waves. As Fig. 13 indicates, oscillations of $\rho^{1/2}w'$ below 44-km altitude have dominant frequencies less than the Brunt–Väisälä frequency N, indicative of gravity waves in the stable layer. Gravity wave frequencies in the stable layer range from $\omega = 1.5 \times 10^{-3}$ to $\omega = 9.0 \times 10^{-3}$ s^{-1} (periods of ~12–70 min) with the strongest oscillation (in the middle of the stable layer near 40-km altitude) at a frequency of 4.8×10^{-3} s^{-1} (22-min period). Fluctuations in the penetrative region (~43–47 km altitude) have a much broader range of frequencies, although the frequency with the largest power at 46-km altitude does coincide with N (25-min period). The presence of significant power in the penetrative region at frequencies larger than N suggests short timescale atmospheric dy-

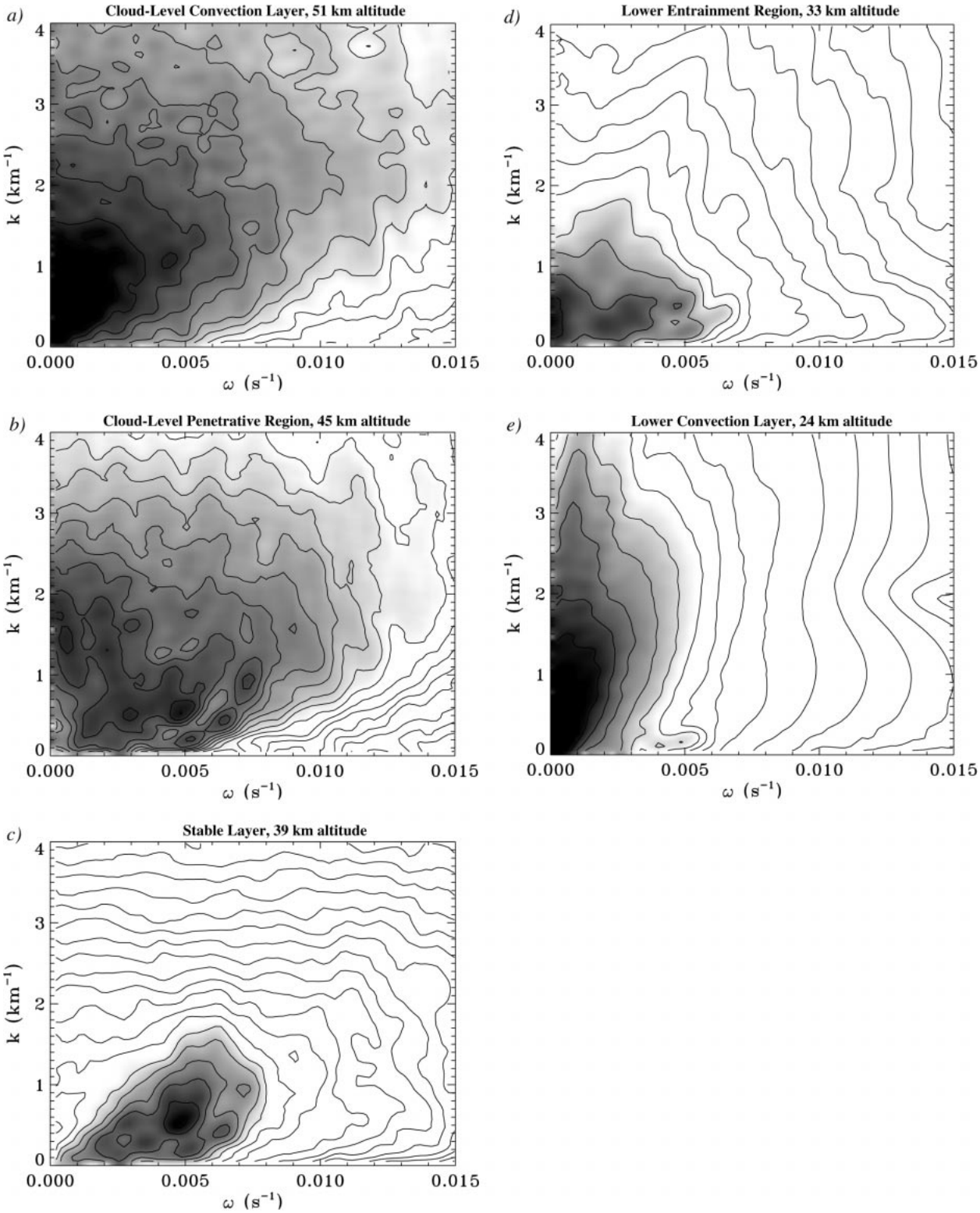

FIG. 12. Two-dimensional spectral energy density of $\rho^{1/2}w'$ as a function of angular frequency ω and horizontal wavenumber k at altitudes of (a) 51, (b) 45, (c) 39, (d) 33, and (e) 24 km. Dark shading indicates regions of large power. The logarithm (base 10) of spectral energy density is plotted with contour intervals of 0.75. The units of spectral energy density are J m^{-3}.

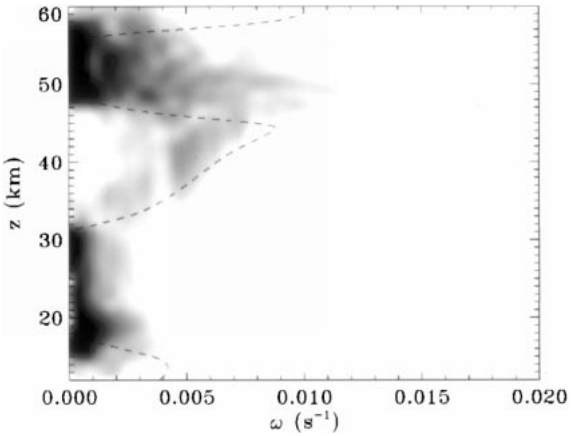

FIG. 13. Power spectral energy density of $\rho^{1/2}w'$ at $x = 60$ km as a function of angular frequency ω and altitude z. The quantity $\rho^{1/2}w'$ was sampled roughly every 100 s from $t = 16.6$ to $t = 32.4$ h. The logarithm (base 10) of spectral energy density is shown here. The units of spectral energy density are J m^{-3}. Dark shading depicts regions of large power. The dashed line is the time-averaged, horizontally averaged Brunt–Väisälä frequency.

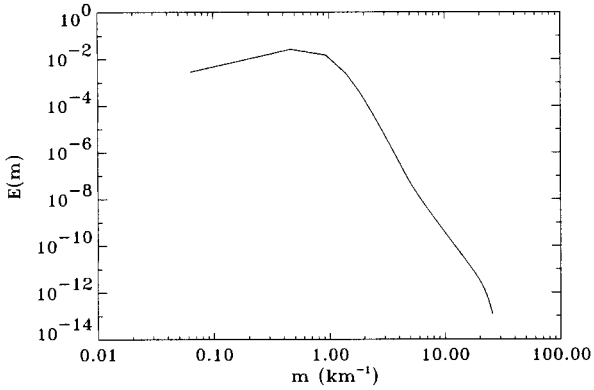

FIG. 14. Time-averaged, horizontally averaged power spectral energy density of $\rho^{1/2}w'$ in the stable layer from 31- to 45-km altitude as a function of vertical wavenumber m.

namics other than linear internal gravity waves. These rapid fluctuations are associated with relatively small length scales (Fig. 12b) and represent small-scale mixing within the penetrative region.

Phase speeds of internal gravity waves depend on the gravity wave source (Lindzen 1981). The intrinsic horizontal phase speed $c_x = \omega/k$ of gravity waves in the stable layer can be determined from Fig. 12c. The largest 2D spectral power at 39-km altitude occurs at $\omega = 4.8 \times 10^{-3}$ s^{-1} and $k = 0.52$ km^{-1}, which gives a dominant phase speed of 9.2 m s^{-1}. Visual tracking of peaks in residual potential temperature also reveals horizontal phase speeds of roughly 10 m s^{-1}. These phase speeds are similar in magnitude to downdraft velocities (9–13 m s^{-1}) near the bottom of the cloud-level convection layer. Thus, internal gravity waves in the stable layer are primarily generated by cloud-level penetrative convection when strong mean wind shear is absent.

In this simulation, gravity wave generation by convection occurs via the ''mechanical oscillator'' effect (Fovell et al. 1992). Cloud-level convective downdrafts, impinging on the interface between the cloud-level convection layer and the underlying stable layer, displace stable air and thus excite internal gravity waves. A second type of wave generation by convection, the ''obstacle'' effect (Clark et al. 1986; Fovell et al. 1992), is not present in the current simulation. The obstacle effect occurs in the presence of mean wind shear: convective plumes act as temporary mountains and deflect horizontally travelling air parcels vertically. Gravity waves generated by the obstacle effect are similar in nature to gravity waves generated by topography (e.g., Young et al. 1994). Because the mean wind in the current simulation is zero, gravity waves are generated through the mechanical oscillator effect alone. Gravity wave generation by the obstacle effect is considered in the companion paper (Baker et al. 2000).

2) COMPARISON WITH OBSERVATIONS

Simulated wave motions in the principal stable layer exhibit potential temperature amplitudes of about 0.1–0.6 K (Fig. 4). In addition, horizontal velocity amplitudes u'' range from 0.4–2.1 m s^{-1} and vertical velocity amplitudes w'' are roughly 0.2–1.0 m s^{-1}. The simulated gravity wave amplitudes are small compared to (but within the lower bounds of) observed wave amplitudes in the stable layer by Pioneer Venus ($u'' \approx 2$–4 m s^{-1}) and Magellan spacecraft ($T'' \approx 0.5$–1.5 K) (Seiff et al. 1980; Counselman et al. 1980; Hinson and Jenkins 1995). Venera 9 and 10 probes also detected vertical velocity oscillations in the stable layer with amplitudes of ~0.3–0.5 m s^{-1} (Kerzhanovich and Marov 1983). Simulated wave amplitudes in the calculation without mean wind shear agree well with the Venera 9 and 10 observations.

Figure 14 shows the spectral energy density of $\rho^{1/2}w'$ in the stable layer from 31- to 45-km altitude as a function of vertical wavenumber m. Vertical power spectra within the stable layer were taken at every horizontal location and then averaged in space and time. Spectra were calculated below 45-km altitude to reduce the nonlinear signal of penetrative dynamics in determining the vertical length scales of internal gravity waves. Internal gravity waves in the stable layer have average vertical wavelengths of 7–14 km ($m = 0.45$–0.90 km^{-1}). The calculated vertical wavelengths are consistent with observations of wave features in the stable layer from Pioneer Venus with vertical wavelengths of 6–7.5 km (Seiff et al. 1980; Counselman et al. 1980), with Venera 9 and 10 vertical wavelengths of 10–15 km (Kerzhanovich and Marov 1983), and with recent Magellan radio

scintillation experiments exhibiting vertical wavelengths of 5–10 km (Hinson and Jenkins 1995).

4. Discussion

A simulation of deep convection and convectively generated gravity waves in the absence of mean wind shear has been performed. The calculation spans from 12- to 60-km altitude and includes two convection layers from 17- to 31-km altitude and from 47- to 56-km altitude, respectively. Internal gravity waves are generated by convection in the stable layer between these two convection layers. Wave motions in the stable layer occur at frequencies less than the Brunt–Väisälä frequency, and vertical velocity and potential temperature fluctuations are roughly 90° out of phase. These characteristics are indicative of propagating internal gravity waves. Cloud-level penetrative convection is the primary wave generation mechanism. Intrinsic horizontal phase speeds ($\sim$10 m s^{-1}) of gravity waves in the stable layer are comparable to cloud-level convective downdraft velocities ($\sim$9–13 m s^{-1}). The characteristic timescale of lower atmosphere convection is two to three times longer than cloud-level convection (convective velocities are two to three times smaller in the lower layer). Without mean wind shear, there is no effective coupling between the lower atmosphere below 34-km altitude and the overlying stable layer. Gravity wave generation by cloud-level convection occurs through the mechanical oscillator effect in which convective downdrafts impinging on the underlying stable layer induce buoyancy oscillations below. Convectively generated internal gravity waves due to the mechanical oscillator effect have characteristic horizontal wavelengths of $\sim$10–15 km and dominant periods of 18–25 min. The waves are vertically trapped by the two convection layers with horizontal wave propagation in both directions.

Interaction between the two convection layers in the absence of mean wind shear is minimal. Average cloud-level penetration extends down to roughly 43-km altitude, while lower-atmosphere entrainment reaches up to 34-km altitude. However, the value of eddy diffusion used in this simulation is 155 m^2 s^{-1}, an upper bound on turbulent diffusion by small-scale eddies in Venus's atmosphere (Leroy 1994). If a smaller value of eddy diffusion were used, the Rayleigh numbers in the convection layers would increase and more vigorous convection would ensue. Convective penetration and entrainment would be stronger (Baker et al. 1999), and the convection layers could be connected by deep penetration from the cloud region and strong entrainment from the lower atmosphere. Furthermore, more vigorous convection would generate internal gravity waves with potentially larger phase speeds since gravity wave phase speeds are closely related to convective velocities. Indeed, changes in the characteristic length scales and timescales of cloud-level convection would naturally result in different gravity wave characteristics in the underlying stable layer.

Although the simulation considers wave generation at the subsolar point, convectively generated internal gravity waves in the simulation match observations at various locations around the planet. Pioneer Venus probe measurements occurred in the early morning at both low and high latitudes (Seiff et al. 1980), Venera 9 and 10 probes sampled near the subsolar region (Kerzhanovich and Marov 1983), and Magellan radio occultation experiments detected temperature oscillations at high latitudes (Jenkins et al. 1994; Hinson and Jenkins 1995). In the absence of mean wind shear, simulated internal gravity waves have horizontal velocity amplitudes of 0.4–2.1 m s^{-1}, vertical velocity amplitudes of roughly 0.2–1.0 m s^{-1}, potential temperature amplitudes of 0.1–0.6 K, and vertical wavelengths of 7–14 km. The wave amplitudes and vertical wavelengths exhibited in the simulation are consistent with observed amplitudes and vertical wavelengths in the stable layer by Pioneer Venus, Venera 9 and 10, and Magellan spacecraft (Seiff et al. 1980; Counselman et al. 1980; Kerzhanovich and Marov 1983; Hinson and Jenkins 1995). This agreement with ''global'' observations suggests two possibilities. First, if observed gravity waves are generated by local convection, wave forcing is similar in magnitude around the planet. This scenario seems unlikely since convective vigor should vary considerably. Second, the observed wave features may be generated by intense convection in the subsolar region. Gravity waves in the stable layer from 31- to 47-km altitude are vertically trapped by the two convection layers. Wave dissipation by thermal radiation will be small in the stable layer (Pollack and Young 1975), and therefore internal gravity waves generated near the subsolar point may propagate horizontally great distances on Venus. Horizontal propagation of convectively generated gravity waves could transfer momentum and energy to other regions on the planet and influence the general circulation away from the subsolar region (Gierasch 1987; Schinder et al. 1990). However, wave dispersion and mechanical dissipation may limit horizontal propagation of internal gravity waves, especially if local regions of large shear and turbulence are encountered.

The Pioneer Venus probes provided reliable atmospheric data down to 12-km altitude, the altitude of the lower boundary in our simulation. The detailed thermal structure of the Venus atmosphere below 12-km altitude is uncertain. Data from the VEGA-2 lander suggest that an unstable planetary boundary layer (PBL) exists from the surface to 6-km altitude with an overlying stable layer from 6- to 18-km altitude (Young et al. 1987). Convection from the PBL could penetrate the overlying stable layer and generate internal gravity waves. If penetration is sufficiently strong, significant interaction between the PBL and the lower convection layer from 18- to 30-km altitude could result. This possibility may be more likely in mountainous regions, such as Aphrodite

Terra, that extend 4 km above the surface (i.e., the PBL could extend to higher altitudes in mountainous regions).

The treatment of thermal radiation in our model is somewhat simplistic. The radiative timescale in the lower atmosphere of Venus is much longer than the timescale of convection and gravity waves, yet thermal radiation plays an important role in determining the thermal structure of the lower atmosphere. Below 60-km altitude, Venus's atmosphere is radiatively opaque and therefore acts as a diffusive process. The value of eddy diffusivity in our model is larger than the radiative diffusivity below 60-km altitude. Indeed, subgrid-scale diffusivity in our model could be viewed to include both turbulent and radiative effects. Nevertheless, a more complete treatment of thermal radiation is necessary, especially given that thermal radiation may be a primary forcing mechanism of convection on the nightside of Venus (Ingersoll et al. 1987; Baker et al. 1999).

The presence of mean wind shear could dramatically influence gravity wave characteristics within the stable layer. Convective plumes could act as obstacles to the mean flow and thus generate gravity waves akin to mountain waves. This wave generation mechanism does not occur in the absence of mean wind shear. Second, critical levels could absorb wave momentum and energy, and significant wave–mean flow interaction could ensue. The influence of mean wind shear on convectively generated internal gravity waves is considered in Part II of this study.

Acknowledgments. The calculation was performed on the San Diego Supercomputing Center (SDSC) Cray T3E. This work was supported by NASA Planetary Atmospheres Program under Grant NAG5-4117.

REFERENCES

Asselin, R., 1972: Frequency filter for time integrations. *Mon. Wea. Rev.,* **100,** 487–490.

Baker, R. D., and G. Schubert, 1992: Cellular convection in the atmosphere of Venus. *Nature,* **355,** 710–712.

——, ——, and P. W. Jones, 1998: Cloud-level penetrative compressible convection in the Venus atmosphere. *J. Atmos. Sci.,* **55,** 3–18.

——, ——, and ——, 1999: High Rayleigh number compressible convection in Venus' atmosphere: Penetration, entrainment, and turbulence. *J. Geophys. Res.,* **104,** 3815–3832.

——, ——, and ——, 2000: Convectively generated internal gravity waves in the lower atmosphere of Venus. Part II: Mean wind shear and wave–mean flow interaction. *J. Atmos. Sci.,* **57,** 200–215.

Beer, T., 1974: *Atmospheric Waves.* John Wiley and Sons, 300 pp.

Clark, T. L., T. Hauf, and J. P. Kuettner, 1986: Convectively forced internal gravity waves: Results from two-dimensional numerical experiments. *Quart. J. Roy. Meteor. Soc.,* **112,** 899–925.

Counselman, C. C. I., S. A. Gourevitch, R. W. King, G. B. Loriot, and E. S. Ginsberg, 1980: Zonal and meridional circulation of the lower atmosphere of Venus determined by radio interferometry. *J. Geophys. Res.,* **85,** 8026–8030.

Fovell, R., D. Durran, and J. R. Holton, 1992: Numerical simulations of convectively generated stratospheric gravity waves. *J. Atmos. Sci.,* **49,** 1427–1442.

Gierasch, P. J., 1987: Waves in the atmosphere of Venus. *Nature,* **328,** 510–512.

——, and Coauthors, 1997: The general circulation of the Venus atmosphere: An assessment. *Venus II,* S. W. Bougher, D. M. Hunten, and R. J. Phillips, Eds., University of Arizona Press, 459–500.

Hinson, D. P., and J. M. Jenkins, 1995: Magellan radio occultation measurements of atmospheric waves on Venus. *Icarus,* **114,** 310–327.

Hou, A. Y., and B. F. Farrell, 1987: Superrotation induced by critical-level absorption of gravity waves on Venus: An assessment. *J. Atmos. Sci.,* **44,** 1049–1061.

——, and R. M. Goody, 1989: Further studies of the circulation of the Venus atmosphere. *J. Atmos. Sci.,* **46,** 991–1001.

Hurlburt, N. E., J. Toomre, and J. M. Massaguer, 1984: Two-dimensional compressible convection extending over multiple scale heights. *Astrophys. J.,* **282,** 557–573.

Ingersoll, A. P., D. Crisp, A. W. Grossman, and the VEGA Balloon Science Team, 1987: Estimates of convective heat fluxes and gravity wave amplitudes in the Venus middle cloud layer from VEGA balloon measurements. *Adv. Space Res.,* **7** (12), 343–1 349.

James, E. P., O. B. Toon, and G. Schubert, 1997: A numerical microphysical model of the condensational Venus cloud. *Icarus,* **129,** 147–171.

Jenkins, J. M., P. G. Steffes, D. P. Hinson, J. D. Twicken, and G. L. Tyler, 1994: Radio occultation studies of the Venus atmosphere with the Magellan spacecraft 2. Results from the October 1991 experiments. *Icarus,* **110,** 79–94.

Kerzhanovich, V. V., and M. Y. Marov, 1983: The atmospheric dynamics of Venus according to Doppler measurements by the Venera entry probes. *Venus,* D. M. Hunten et al., Eds., University of Arizona Press, 766–778.

Krasnopolsky, V. A., 1985: Chemical composition of Venus clouds. *Planet. Space Sci.,* **33,** 109–117.

——, and V. A. Parshev, 1981: Chemical composition of the atmosphere of Venus. *Nature,* **292,** 610–613.

——, and ——, 1983: Photochemistry of the Venus atmosphere. *Venus,* D. M. Hunten et al., Eds., University of Arizona Press, 431–458.

Leroy, S. S., 1994: Convectively generated internal gravity waves in Venus's middle atmosphere: Momentum transport and radio scintillations. Ph.D. thesis, California Institute of Technology, 204 pp. [Available from California Institute of Technology, Pasadena, CA 91125.]

——, and A. P. Ingersoll, 1995: Convective generation of gravity waves in Venus's atmosphere: Gravity wave spectrum and momentum transport. *J. Atmos. Sci.,* **52,** 3717–3737.

——, and ——, 1996: Radio scintillations in Venus's atmosphere: Application of a theory of gravity wave generation. *J. Atmos. Sci.,* **53,** 1018–1028.

Lindzen, R. S., 1981: Turbulence and stress owing to gravity wave and tidal breakdown. *J. Geophys. Res.,* **86,** 9707–9714.

Pollack, J. B., and R. Young, 1975: Calculations of the radiative and dynamical state of the Venus atmosphere. *J. Atmos. Sci.,* **32,** 1025–1037.

Schinder, P. J., P. J. Gierasch, S. S. Leroy, and M. D. Smith, 1990: Waves, advection, and cloud patterns on Venus. *J. Atmos. Sci.,* **47,** 2037–2052.

Schubert, G., 1983: General circulation and the dynamical state of the Venus atmosphere. *Venus,* D. M. Hunten et al., Eds., University of Arizona Press, 681–765.

——, and R. L. Walterscheid, 1984: Propagation of small-scale acoustic-gravity waves in the Venus atmosphere. *J. Atmos. Sci.,* **41,** 1202–1213.

Seiff, A., 1983: Thermal structure of the atmosphere of Venus. *Venus,* D. M. Hunten et al., Eds., University of Arizona Press, 215–279.

——, D. B. Kirk, R. E. Young, R. C. Blanchard, J. T. Findlay, G. M. Kelly, and S. C. Sommer, 1980: Measurements of thermal structure and thermal contrasts in the atmosphere of Venus and related dynamical observations: Results from the four Pioneer Venus probes. *J. Geophys. Res.*, **85,** 7903–7933.

——, R. E. Young, R. Haberle, and H. Houben, 1992: The evidences of waves in the atmospheres of Venus and Mars. *Venus and Mars: Atmospheres, Ionospheres, and Solar Wind Interactions, Geophys. Monogr.*, No. 66, Amer. Geophys. Union, 73–89.

Staley, D. O., 1970: The adiabatic lapse rate in the Venus atmosphere. *J. Atmos. Sci.*, **27,** 219–223.

Stull, R. B., 1988: *An Introduction to Boundary Layer Meteorology*. Kluwer Academic, 666 pp.

Tomasko, M. G., L. R. Doose, P. H. Smith, and A. P. Odell, 1980: Measurements of the flux of sunlight in the atmosphere of Venus. *J. Geophys. Res.*, **85,** 8167–8186.

Young, R. E., R. L. Walterscheid, G. Schubert, A. Seiff, V. M. Linkin, and A. N. Lipatov, 1987: Characteristics of gravity waves generated by surface topography on Venus: Comparison with the VEGA balloon results. *J. Atmos. Sci.*, **44,** 2628–2639.

——, ——, ——, L. Pfister, H. Houben, and D. L. Bindschadler, 1994: Characteristics of finite amplitude stationary gravity waves in the atmosphere of Venus. *J. Atmos. Sci.*, **51,** 1857–1875.

Yung, Y. L., and W. B. Demore, 1982: Photochemistry of the stratosphere of Venus: Implications for atmospheric evolution. *Icarus*, **51,** 199–247.